MATERIALS SCIENCE

Understanding charge transport in lead iodide perovskite thin-film field-effect transistors

Satyaprasad P. Senanayak,[1]*† Bingyan Yang,[1]† Tudor H. Thomas,[1] Nadja Giesbrecht,[2] Wenchao Huang,[3] Eliot Gann,[3] Bhaskaran Nair,[4] Karl Goedel,[1] Suchi Guha,[5] Xavier Moya,[4] Christopher R. McNeill,[3] Pablo Docampo,[2,6] Aditya Sadhanala,[1] Richard H. Friend,[1] Henning Sirringhaus[1]*

Fundamental understanding of the charge transport physics of hybrid lead halide perovskite semiconductors is important for advancing their use in high-performance optoelectronics. We use field-effect transistors (FETs) to probe the charge transport mechanism in thin films of methylammonium lead iodide ($MAPbI_3$). We show that through optimization of thin-film microstructure and source-drain contact modifications, it is possible to significantly minimize instability and hysteresis in FET characteristics and demonstrate an electron field-effect mobility (μ_{FET}) of 0.5 cm^2/Vs at room temperature. Temperature-dependent transport studies revealed a negative coefficient of mobility with three different temperature regimes. On the basis of electrical and spectroscopic studies, we attribute the three different regimes to transport limited by ion migration due to point defects associated with grain boundaries, polarization disorder of the MA^+ cations, and thermal vibrations of the lead halide inorganic cages.

INTRODUCTION

Hybrid organic-inorganic perovskites, such as methylammonium lead iodide ($CH_3NH_3PbI_3$; hereafter $MAPbI_3$), represent a previously unknown class of semiconductors for a wide range of optoelectronic applications. These materials exhibit interesting properties such as high absorption coefficient (*1*), tunable bandgap (*2*), and high photoluminescence quantum yield (*3*). Despite low-temperature (≤100°C) solution processing, the density of electronic defect states is surprisingly low, hence it has been possible to realize solar cells with efficiencies of more than 20% (*4*), color-pure light-emitting diodes (*3*, *5*), and optically pumped lasing (*6*, *7*). On the basis of impressive device performance and superior optoelectronic properties, such as clean band structure (*8*, *9*), high degree of crystallinity (*10*), and low effective mass of charge carriers comparable to inorganic semiconductors such as GaAs and Si (*11*), the charge mobility of these materials is generally regarded as "high." Measurements of the carrier mobilities on single crystals using terahertz (THz) techniques have yielded values of up to 100 cm^2/Vs (*12*), which are higher than conventional organic semiconductors but modest compared with inorganic semiconductors that exhibit similar high performance in solar cells (*13*). However, many aspects of the charge transport, such as the mechanism of carrier scattering and trapping, the role of ion migration, the origin of hysteresis in the device characteristics, and the electronic structure of grain boundaries in these hybrid perovskites, particularly for polycrystalline thin films, remain unexplored.

Field-effect transistors (FETs) provide a versatile platform to study the charge transport mechanism of semiconductors in a controlled manner. In addition to determining field-effect mobility (μ_{FET}), FETs allow precise electrical control of the charge density and have yielded valuable insight into the transport physics of organic (*14*, *15*) and inorganic semiconductors (*16*), including tin-based two-dimensional (2D) perovskites (*17*) with a μ_{FET} of ~0.6 cm^2/Vs. However, the fabrication of FETs with the 3D perovskites, such as $MAPbI_3$, has remained challenging (*18*–*23*). A major difficulty has been ion migration, which causes a partial screening of the applied gate field, yielding a very low room temperature μ_{FET} of 10^{-4} cm^2/Vs in thin films of $MAPbI_3$ (*18*). Li *et al.* (*19*) reported perovskite phototransistors that owed their high photoresponsivity to a very poor transistor performance in the dark, which substantially improved upon light illumination. Furthermore, the reported perovskite FETs are prone to degradation during operation over multiple cycles and exhibit significant hysteresis in their current-voltage characteristics (*20*). Even in single-crystal devices, strong hysteresis and moderate mobilities of $<10^{-3}$ cm^2/Vs were reported at room temperature (*21*). This low device performance, at room temperature and in the absence of light, has limited the fundamental insight into the transport physics that could be gained from FET studies and relate it to the observed excellent solar cell performance. To make progress with perovskite FETs, we need to better understand the instabilities in their device characteristics associated with hysteresis and their degradation upon repeated cycling and to develop techniques to reduce their effect and allow sufficiently stable operation not only at low temperatures but also at room temperature. Through the optimization of processing conditions to control thin-film microstructure and the modification of source-drain (S-D) contacts, we are able to fabricate $MAPbI_3$ FETs that exhibit clean electron transport under dark conditions, with significantly reduced instability and hysteresis. This allows us to meaningfully evaluate charge transport across a wide temperature range, from 100 K to room temperature. As a result, we are able to identify different temperature regimes in which different scattering mechanisms and transport-limiting factors manifest themselves.

RESULTS AND DISCUSSION

The choice of the perovskite precursor materials and the technique for their solution deposition controls the polycrystalline microstructure and charge transport properties of $MAPbI_3$ FET thin films (*24*). Here,

[1]Optoelectronics Group, Cavendish Laboratory, University of Cambridge, JJ. Thomson Avenue, Cambridge CB3 0HE, U.K. [2]Department of Chemistry and Center for NanoScience (CeNS), Ludwig-Maximilians-Universität München, Butenandtstraße 11, 81377 München, Germany. [3]Department of Materials Science and Engineering, Monash University, Clayton Campus, Wellington Road, Clayton, Victoria 3800, Australia. [4]Department of Materials Science and Metallurgy, University of Cambridge, 27 Charles Babbage Road, Cambridge CB3 0FS, U.K. [5]Department of Physics and Astronomy, University of Missouri, 223 Physics Building, Columbia, MO 65211–7010, USA. [6]School of Electrical and Electronic Engineering, Newcastle University, Merz Court, Newcastle upon Tyne NE1 7RU, U.K.
†These authors contributed equally to the work.
*Corresponding author. Email: sps54@cam.ac.uk (S.P.S.); hs220@cam.ac.uk (H.S.)

we use a precursor mixture based on $Pb(Ac)_2$ (*25*) that results in compact thin films with uniform coverage, a root mean square (RMS) roughness of ~5.4 nm, and a grain size of 38 nm (Fig. 1A). In contrast, films grown from the more conventional PbI_2-based precursor mixtures exhibit a higher RMS surface roughness of ~114 nm and poorer film coverage for similar grain size and film thickness (fig. S1) (*26*). In addition, a comparison of the x-ray diffraction (XRD) of perovskite films prepared using both methods suggests a lower degree of precursor conversion for the latter with a more intense peak due to residual PbI_2 ($2\theta = 12.5°$) (figs. S2 to S4) (*27*), compared with a near-complete conversion in $Pb(Ac)_2$-based films.

We fabricated bottom-contact, top-gate field-effect transistors with gold S-D contacts and a fluoropolymer gate dielectric (Cytop) using 0.25 M solutions of both PbI_2 and $Pb(Ac)_2$ precursors, which result in perovskite films with a thickness of ~100 nm (*1*). Devices fabricated from the PbI_2 precursor mixtures exhibit very poor, leakage-dominated characteristics, which makes it difficult to estimate the μ_{FET} even at 100 K (fig. S5). In contrast, devices fabricated from the $Pb(Ac)_2$ precursor exhibit much better n-type transport characteristics (Fig. 1C and fig. S6). Despite significant "clockwise" hysteresis in the device characteristics, we can identify linear and saturation regimes in the output characteristics and reliably extract a saturation electron μ_{FET} of ~0.2 ± 0.08 cm^2/Vs and an on/off ratio of ~10^5 (for a detailed discussion of the method of mobility extraction, see section S4). However, upon increasing the temperature to 250 K, μ_{FET} decreases strongly to 0.02 ± 0.01 cm^2/Vs, and the output characteristics exhibit a complex, nonideal behavior without a clean saturation regime (fig. S6B). This behavior bears the signature of ion migration under the action of the applied gate and S-D electric fields (for a detailed discussion, see section S5). No field-induced transport could be observed at room temperature in these perovskite FETs.

To optimize device performance, we investigated the role of the grain size in $MAPbI_3$ thin films by varying the grain size from 38 nm (for our initial devices fabricated from 0.25 M solutions) to 150 nm, with increasing concentration of the $Pb(Ac)_2$ precursor from 0.25 to 1.00 M (Fig. 1B) (details in Materials and Methods). SEM images (Fig. 1A) show the grain size for films prepared with different precursor concentrations. Upon increasing the grain size, the transfer characteristics exhibit an increase in S-D current (I_{ds}) by up to an order of magnitude, resulting in a μ_{FET} of ~0.6 ± 0.2 cm^2/Vs at 100 K and 0.05 ± 0.01 cm^2/Vs at 270 K for a film grown from the 0.75 M concentration (Fig. 1C). As the grain size increases, field-effect transport was observed at room temperature. Typical transfer characteristics of a perovskite FET fabricated from 0.75 M $Pb(Ac)_2$ precursor operating at room temperature is shown in fig. S6F. For devices with large grain size, it was also possible to observe comparatively clean output curves from 100 to 270 K (figs. S6 and S7), with channel currents at least one order of magnitude higher than in devices with smaller grain size. This tendency of increasing μ_{FET} and device stability with grain size suggests that film microstructure plays an important role in device instabilities.

To better understand the enhancement in charge transport with increasing grain size, we performed XRD crystallography analysis on the samples. In fig. S4, we compare grazing incidence wide-angle x-ray scattering (GIWAXS) images of thin films prepared with different precursor concentrations. Perovskite films with smaller grain size exhibit a preferential orientation of crystallites with the (110) direction oriented out of plane. A smaller population of randomly oriented crystallites also exists, evidenced by powder-like diffraction rings. In contrast, films of larger grains (0.75 M) exhibit two different populations of preferentially oriented crystallites, one with the (110) direction oriented out of plane and another with the (110) direction oriented at 45° to the substrate plane. This observation suggests that

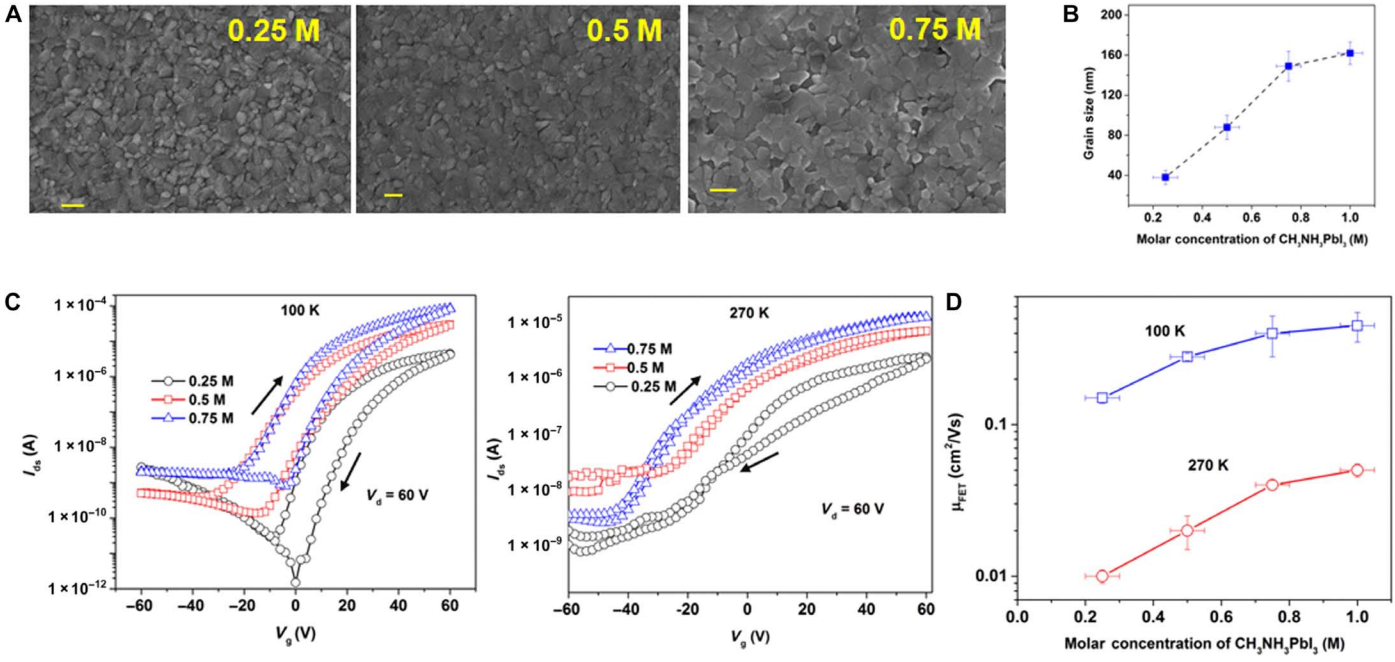

Fig. 1. Effect of grain size on the characteristics of FET devices with gold S-D contacts. (**A**) Scanning electron microscopy (SEM) images of $MAPbI_3$ films fabricated from 0.25, 0.5, and 0.75 M precursor solutions. Scale bars, 200 nm. (**B**) Grain size as a function of concentration of the precursor solution. (**C**) Transfer characteristics at 100 and 270 K for $MAPbI_3$ FETs with channel length (L) = 10 μm and width (W) = 1 mm deposited with different precursor concentrations. (**D**) μ_{FET} as a function of precursor concentration measured from perovskite FETs at 100 and 270 K.

for the different precursor concentrations, there are different growth modes that lead to films with different crystallite orientations. Furthermore, it is evident from the XRD that films with larger grain size exhibit significantly sharper diffraction spots than those with small grain size (inset, fig. S2). Detailed structural analysis of the 0.25 M films by high-resolution XRD (fig. S3) showed strong perovskite peaks at 2θ = 14.1°, 28.4°, and 43.2° assigned to (110)/(002), (220)/(004), and (330)/(006), respectively, in the out-of-plane direction, confirming the well-known tetragonal (I4/mcm) phase with lattice parameters $a = b$ = 8.86 Å and c = 12.57 Å, as determined by a full Rietveld refinement. This agrees with the literature for perovskite thin films (*9*).

The absence of certain predicted reflections indicates a strong degree of preferential orientation of the crystallites, in agreement with our GIWAXS findings. The Bragg peak at 12.5°, which corresponds to unconverted PbI_2, is more intense by a factor of 5 in the 0.25 M film compared with the 0.75 M one (fig. S2). This correlates well with the decrease in grain size (or increase in the area of grain boundaries) by a factor of approximately 4, which may suggest that the unconverted PbI_2 is predominantly phase-segregated from the perovskite and is instead located at or near grain boundaries (*28*). A confirmation of the phase segregation between perovskite and PbI_2 is obtained by fitting the peak assigned to the impurity of PbI_2 ($P\bar{3}m1$) with the published lattice parameters $a = b$ = 4.575 Å and c = 7.0357 Å. This clear correlation between microstructure and device performance suggests that the improved transport characteristics in the 0.75 M films at room temperature may at least partly be attributed to a lower concentration of PbI_2 located between grains, resulting in reduced migration of ions arising from point defects at grain boundaries that screen the applied gate voltage. This will be discussed in more detail below.

To further improve room temperature FET characteristics, we modified the gold S-D contacts with the self-assembled monolayer (SAM) pentafluorobenzenethiol (PFBT; ~1 nm thick) and the polymer surface modification layer polyethylenimine ethoxylated (PEIE; ~2 nm thick) (*29*), which increase and decrease the gold work function, respectively. In Fig. 2A, we compare the transfer characteristics of perovskite devices fabricated with bare gold electrodes with those modified with different SAM layers. The introduction of these interlayers results in an increase of the I_{ds} in both cases, and correspondingly, a μ_{FET} of 1 to 2.5 cm^2/Vs is observed at 100 K. Specifically, the PEIE contact modifications reduced the hysteresis in the transfer characteristics measured in pulsed gate voltage mode at room temperature to a much smaller level (Fig. 2B) that allowed reliable extraction of transport parameters at room temperature.

The room temperature μ_{FET} increases from 0.02 ± 0.01 cm^2/Vs for bare gold contacts to 0.1 to 0.5 cm^2/Vs for PEIE-treated electrodes (fig. S8 shows the mobility distribution statistics). In champion PEIE-treated devices, μ_{FET} values as high as 5 cm^2/Vs at 100 K and 3 cm^2/Vs at room temperature were observed, which approach, within an order of magnitude, the local mobility estimates from THz (*12*) and microwave conductivity (*30*) measurements. Furthermore, upon PEIE treatment of contacts, it became possible to obtain an output curve at room temperature (Fig. 2D). Generally, a mismatch in the magnitude of I_{ds} is observed between the output and transfer characteristics under the same S-D (V_d) and gate (V_g) potentials, which reflects an instability of the device current depending on the different measurement sequences. We define the I_{ds} mismatch parameter (ξ) $\equiv I_{ds}^{transfer}/I_{ds}^{output}$ under the same voltage condition (here, $V_d = V_g$ = 60 V); for a perfectly stable FET, ξ is expected to be 1. In 0.75 M perovskite FETs with bare gold contacts, ξ increases from ≈ 2 to 100 as the temperature is raised from 100 to 270 K. However, for devices with treated contacts, the mismatch is comparatively small, increasing from $\xi \approx 1.2$ to 2 for PEIE and from $\xi \approx 1.5$ to 10 for PFBT between 100 and 300 K, thus indicating that a moderately thick interlayer is needed to maximize device stability (fig. S13E). Devices with PEIE-modified electrodes exhibit significantly enhanced and more stable operational characteristics near room temperature compared to those with unmodified contacts (section S8).

To understand the mechanism for the observed enhancement in transport properties with different interlayers, we first note that the observed improvement in room temperature operation with contact modification cannot be explained by work function/electron injection barrier arguments because both PFBT- and PEIE-modified contacts exhibit this improvement (fig. S13). To investigate the role of the microstructure, we performed SEM imaging of the channel region (figs. S14 to S15). These measurements indicate further increase in the grain size of the perovskite thin films inside the channel region from 150 nm for bare gold contacts to <200 nm for treated electrodes. This is possibly driven by the contact-induced enhanced nucleation of the perovskite and its crystallization into confined channel regions, which could be attributed to the enhanced halogen-halogen or amine-amine interaction from PFBT- and PEIE-treated electrodes, respectively; similar effects have previously been observed for organic FETs (*31*, *32*). Thus, although there may well be effects of interfacial electronic structure or electrochemical reactions that contribute to the improved performance by contact modification, the effects of contact-induced changes in film microstructure and grain size in the channel are likely to be an important contributing factor.

The optimized devices exhibit stable operation and can be measured over multiple cycles and bias stressed for periods of 30 min without significant changes in current or hysteresis behavior (figs. S17 to S19). These rather reproducible characteristics allowed us to more systematically investigate the origin of the residual hysteresis, which depends strongly on temperature and measurement conditions. The output curves (Fig. 2, C and D) display hysteresis over the complete temperature range, showing that hysteresis increases with increasing gate voltage and temperature. However, the transfer characteristics exhibit significant hysteresis only at low temperature, which decreases at room temperature (Fig. 2, A and B).

The difference in hysteresis behavior between the output and transfer characteristics arises from the difference in the transfer and output characteristic measurement sequences (details in Materials and Methods). In the transfer scans, V_g is pulsed, whereas V_d is held constant; in the output scans, V_d is pulsed, whereas V_g is maintained at a constant bias. A comparison between Figs. 2B and 2D shows that when near room temperature (T > 240 K, as shown in a later section), the hysteresis is primarily induced by the applied gate voltage. This becomes evident when the transfer curves were measured by applying both V_d and V_g in a continuous mode where a large hysteresis is observed, particularly near room temperature (fig. S20). This suggests that at T > 240 K, the observed clockwise hysteresis between forward and reverse characteristics can be ascribed to the gate voltage–induced migration of ions or charged point defects in the perovskite. When negatively (positively) charged point defects drift toward (away from) the interface under application of a positive gate voltage, they screen the applied gate electric field and reduce the concentration of mobile electrons in the accumulation layer of the FET. Further evidence of the ionic defect migration affecting the field-effect behavior is obtained

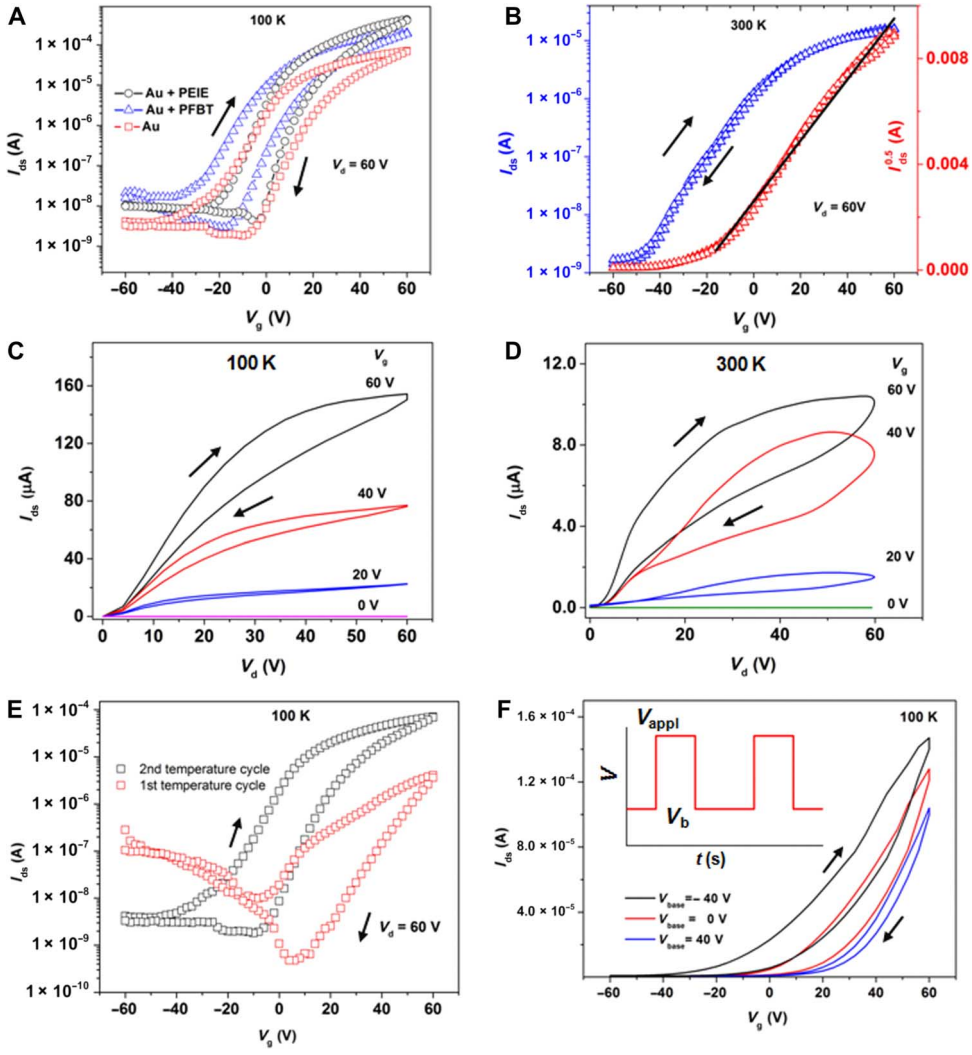

Fig. 2. Electrical characterization of $MAPbI_3$ FETs with different S-D contact modifications. Transfer characteristics at (**A**) 100 K for different S-D contact modification and (**B**) 300 K for PEIE-treated Au contacts. Also shown is the square root of I_{ds} and the linear fit over a large positive V_g range. Output characteristics of FETs with PEIE-treated Au S-D contacts at (**C**) 100 K and (**D**) 300 K (L = 20 μm and W = 1 mm). (**E**) Transfer characteristics measured at 100 K upon thermal cycling. (**F**) Effect of the base voltage variation on the transconductance plots for the same FET. The inset shows a schematic diagram of the pulse voltage. For all devices, we used a 0.75 M precursor concentration.

from the measurements on a dual gate transistor with a Cytop top gate and Si/SiO_2 bottom electrodes as the control gate. It was possible to regulate the defect screening of gate potential by varying the bias at the back gate, and consequently, a clear tunability of transport from a bulk space charge limited behavior to a clean field modulated saturated behavior is obtained (for detailed discussion, see section S5).

However, at low temperatures, the origin of hysteresis behavior must be different; even when measured in pulsed gate voltage mode, the transfer characteristics retain hysteresis at 100 K. This would not be expected from ion migration because ion migration is expected to slow down at low temperature, which should make it easier, not harder, to avoid hysteresis effects by gate voltage pulsing. Furthermore, the transfer curves at low temperatures exhibit a similar degree of hysteresis independent of the grain size (Fig. 1C), whereas, as discussed above, the room temperature device performance clearly indicated more pronounced ion migration in films with small grain size. It is expected that ion migration is becoming increasingly less important for temperatures below 240 K (also shown by the impedance spectroscopy below) because the diffusion of charged point defects is a strongly temperature-activated process. Typical activation energies of 0.58, 0.84, and 2.31 eV have been calculated for iodide (V_I^+), methylammonium (V_{MA}^-), and lead (V_{Pb}^{2-}) vacancies, respectively (*33*, *34*). Considering a typical Boltzmann probability, the diffusion coefficient of the most mobile iodine vacancies would be expected to decrease by a factor of 10^5 between room temperature and 100 K. This suggests that at low temperature, the hysteresis might have a different origin and is not dominated by ion migration.

To better understand the origin of the low-temperature hysteresis, we analyzed possible sources for hysteresis such as ferroelectricity (*35*–*37*). Ferroelectric polarization measurements performed on perovskite thin films at different temperatures and frequencies (fig. S21) did not show any evidence of a clear ferroelectric loop. We also performed transfer characteristic measurements with varying base gate voltage (V_b) to which the gate voltage was switched in between the pulsed

measurements (inset, Fig. 2F). It was possible to significantly reduce the hysteresis by choosing V_b = 40 V while only decreasing the on current at V_g = 60 V by less than 30%. This is not expected for a hysteresis mechanism based on ion migration because a positive applied V_b is expected to significantly increase the amount of gate voltage screening. The dependence on V_b and particularly the strongly negative onset voltages for negative V_b can be more readily explained by an electronic mechanism based on injection and trapping of holes in the perovskite under negative V_g followed by recombination with electrons that are injected into the channel as the gate voltage is swept to positive voltages. The ensuing hysteresis is expected to be less severe if V_b is kept positive and hole injection is minimized. In addition, we also observe that the low-temperature hysteresis in the transfer plot increases with high-*k* dielectrics like polymethyl methacrylate (PMMA), indicating a possible trap-dominated electronic mechanism for the hysteresis (fig. S22).

One further interesting aspect of the electrical characteristics of our perovskite FETs is an observed enhancement in device performance upon thermal cycling. On the second cooling-heating cycle, the temperature-dependent device characteristics were significantly improved (by up to two orders of magnitude) compared to the first cycle (Fig. 2E and section S12). All transistor characteristics presented here, except when stated otherwise, are from the second cooling cycle after the device has undergone one complete cycle of cooling to 100 K and warming up. Corresponding enhancement in the output characteristics on thermal cycling is shown in fig. S24.

To isolate the effects of applied bias and thermal cycling, we performed transfer measurements independently under the effect of bias and thermal cycling (section S12). We attribute the observed enhancement to a combination of thermal cycling and electrical biasing, with thermal cycling being the more important factor. In capacitance measurements performed during thermal cycling, we observe evidence for increased polarization order of the MA^+ cations (fig. S28) and the structural analysis. Correspondingly, the energetic disorder quantified by the Urbach energy (E_u; estimated from the tail state absorption) was observed to decrease by around 1 meV (fig. S29). Furthermore, structural analysis of the thin films upon thermal cycling indicates a relative decrease of the unconverted PbI_2 peak (fig. S30). From this analysis, it is evident that both polarization order as well as the decrease in point defect densities improve during thermal cycling.

The device instabilities discussed above clearly complicate the understanding of the underlying transport physics of the perovskite. However, we have mitigated these instabilities to a level where a meaningful investigation of the $\mu_{FET}(T)$ behavior of perovskite FETs fabricated from films with varied grain size and different interlayers at the S-D electrodes is possible (Fig. 3). We extracted $\mu_{FET}(T)$ from the saturated transfer characteristics and compared values obtained from the forward and reverse sweeps. As shown earlier, fig. S7 shows examples of mobility extraction from the transfer characteristics at different temperatures. Mobilities extracted from the forward and reverse characteristics differed by no more than 9% at low temperatures, where transconductance plots have larger hysteresis, and up to a maximum of 0.02 cm^2/Vs for room temperature operation. For the plots in Fig. 3, we used the values from the forward characteristics, which tend to be more conservative. In contrast to most other thin-film FETs based on, for example, organic semiconductors or amorphous silicon, where disorder usually leads to a temperature-activated behavior, $\mu_{FET}(T)$ exhibits a clear negative temperature coefficient, that is, an increase in μ_{FET} with decreasing temperature, over the complete temperature range from 100 to 300 K. This is remarkable given the polycrystalline morphology of our thin films and their relatively low mobility compared to theoretically expected values and suggests that either there are very few electronic traps states in the density of states or, more likely, there are strongly temperature-dependent scattering mechanisms that counteract the effect of residual electronic trap states.

We observe three temperature regimes identified from the distinct slopes in the μ_{FET} versus T plots (Fig. 3, A and B), which are analyzed by fitting a typical power law behavior to $\mu_{FET} \sim \mu_0 T^{-\gamma}$. The exponent γ was found to be ranging from 0.2 to 0.4 in the low-temperature regime I (100 K < T < 160 K), from 2.6 to 3.2 in the intermediate-temperature regime II (160 K < T < 250 K), and from 4.1 to 5.3 in the high-temperature regime III (250 K < T < 300 K) (Fig. 3 and fig. S33). The values of the extracted exponent should be considered as indicative only because the individual temperature regimes are too narrow to allow an accurate determination, particularly in regime II. In regime III, there is a clear correlation between the mobility exponent and the film quality, that is, films with smaller grain size exhibit a larger mobility exponent (Fig. 3B).

To obtain insights into the mechanisms that govern the different transport regimes, we performed electrical and optical spectroscopy on our perovskite thin films. Impedance spectroscopy measurements were performed on films sandwiched between two metal gold contacts to probe the sources of polarization (electronic versus ionic) and dielectric relaxation (details in Materials and Methods). Hence, we measured both bulk capacitance (C) (Fig. 4A) and dielectric loss (ε'') (Fig. 4B) as a function of frequency and temperature; all measurements were performed in the dark to avoid the large photocapacitance effects that have previously been reported for these materials (*38*, *39*). The $C(f)$ measurements are shown over a frequency range of 1 kHz to 10 MHz to avoid the superlinear capacitive behavior at low frequency due to the ionic contribution (Fig. 4A and fig. S34) (*38*, *40*).

The dielectric loss spectroscopy results provide clear evidence that in regime III, transport mainly reflects the temperature dependence of ion migration and the associated screening of the gate electric field by negatively charged iodide ions. At 300 K, the dielectric loss spectra exhibit two characteristic relaxation frequencies, a low-frequency component at frequencies of $<10^4$ Hz attributed to ionic relaxation and a high-frequency component (~10^5 to 10^6 Hz), which can be ascribed to an electronic conduction and trapping mechanism in $MAPbI_3$ (Fig. 4B and fig. S34) (*40*, *41*). Upon cooling the perovskite devices to T = 240 K, we observed that the low-frequency component, which we attribute to the ionic relaxation, disappeared, and only the high-frequency electronic relaxation remained. This suggests that at $T \leq$ 240 K, ion migration is effectively suppressed. This is fully consistent with the observation in Fig. 3B that the strong dependence of mobility on microstructure and grain size, which we interpret in terms of different concentrations of charged point defects in the films, only sets in around this temperature; that is, the screening effect of the gate field associated with ion migration can be effectively neglected for T < 240 K, which is consistent with the previous reports of perovskite FETs demonstrated over a temperature range of 77 to 220 K (*18*, *19*).

The dielectric constant $\varepsilon_r = Cd/\varepsilon_o A$ (where C is the capacitance, d is the film thickness, A is the area of the capacitance, and ε_o is the vacuum permittivity) calculated from the capacitance data in Fig. 4A at room temperature is relatively high (ε_r ~ 21 to 23 at 100 kHz) and increases further to values of ~27 to 33 (at 100 kHz) upon cooling to 100 K. We model the dielectric behavior using the standard Kirkwood-Fröhlich equation for polar, orientationally disordered solids. At room

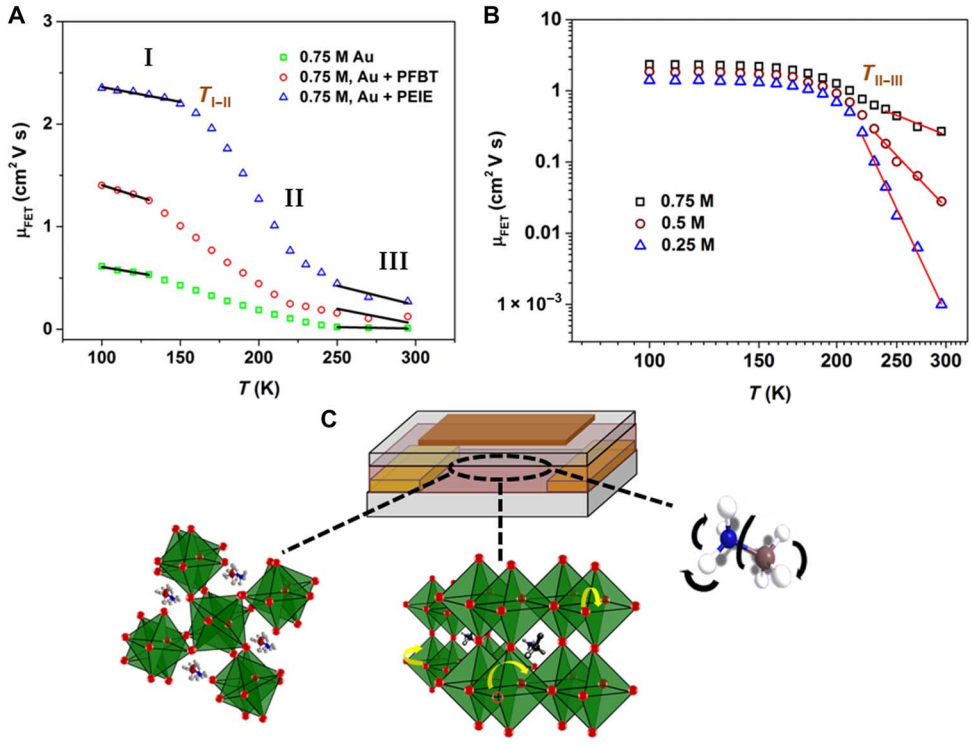

Fig. 3. Temperature-dependent transport measurements on $MAPbI_3$ FETs. (**A**) $\mu_{FET}(T)$ with different interlayers at the S-D contacts depicting three different regimes of charge transport with a power law behavior: $\mu \sim \mu_0 T^{-\gamma}$. Region I: inorganic cage vibrational disorder (γ ~0.2 to 0.4); region II: dominated by the polarization fluctuation of MA^+; region III: dominated by ion migration (γ ~4.1 to 5.3). (**B**) $\mu_{FET}(T)$ from FETs fabricated with different precursor concentration of perovskite solutions and PEIE-modified S-D electrodes. (**C**) Schematic of top-gate bottom-contact perovskite FETs summarizing the different sources of disorder mechanisms prevalent in a perovskite FETs corresponding to different regimes in the $\mu_{FET}(T)$ (left: vibrations of inorganic cage; middle: defect migration; right: MA^+ polarization disorder).

temperature where the entropy associated with the MA^+ orientations is high, we can assume that the Kirkwood correlation factor $g \sim 1$, indicating no specific interaction among the MA^+ cations (*35*). Assuming that the optical dielectric constant of perovskite $\varepsilon_\infty \sim 6.5$ (*42*) and the molar volume (*43*, *44*) is 3.95×10^{27} m^{-3}, we obtain a dipole moment of 1.94 D, which is of comparable magnitude to the dipole moment estimated from ab initio electronic structure calculations (2.1 D).

This reasonable agreement between experiment and theory points to the fact that the dielectric constant measurement reflects mainly the polarization of the MA^+ cation dipole moments (*35*, *41*, *45*). They are disordered near room temperature, but upon lowering the temperature, the thermal disorder in the dipole orientation decreases, which gets reflected as an increase in the dielectric constant (*44*), in agreement with ultrafast vibrational spectroscopy results (*46*). This interpretation is also consistent with measurements of the bulk energetic disorder in our films, obtained from external quantum efficiency measurements in the sub-bandgap region on a perovskite solar cell (with a power conversion efficiency $\eta \sim 11\%$) at different temperatures. As shown in fig. S35, we observe a clear decrease in E_u from 14 meV at 300 K to 9.5 meV at 100 K. This decrease in energetic disorder is consistent with the dielectric spectroscopy and with the negative coefficient of $\mu_{FET}(T)$ (fig. S35E and Fig. 3).

To obtain further spectroscopic signatures of the polarization disorder from MA^+ cations and to better understand the potential contribution of inorganic cage (PbI_6) distortion to the disorder, Raman spectroscopy measurements were performed on perovskite thin films with different grain sizes as well as single crystals. Figure 4C shows typical room temperature Raman spectra with Lorentzian fits to the peaks of the 0.75 M sample shown as an inset. Characteristic peaks corresponding to the PbI_6 cage modes (I-Pb-I bending ~70 cm^{-1} and Pb-I stretching ~90 cm^{-1}) and peaks due to MA^+ motion (libration ~160 cm^{-1} and torsional motion in the range of ~220 to 250 cm^{-1}) were observed (*47*, *48*). Additionally, a strong band centered at ~110 cm^{-1} has been assigned to a coupled mode of cage and MA^+ libration (*47*). Upon increasing the grain size, the Raman peaks assigned to the inorganic cage motion increase in intensity and the peak at 110 cm^{-1} exhibits a relative reduction, indicating, respectively, a higher degree of order and a decrease in the coupling between the inorganic cage and MA^+. These differences are qualitatively similar to those observed previously between "disordered" $MAPbI_3$ films grown on mesoporous substrates and "ordered" $MAPbI_3$ films grown on flat substrates (*48*). Furthermore, upon increasing the grain size, the peak corresponding to the torsional motion of the MA^+ cation undergoes an increase in frequency by around 10 cm^{-1} at room temperature, indicating a stiffening of the MA^+ cation vibration with increased grain size of the perovskite films (*47*, *49*). From both structural analysis and Raman measurements, we conclude that the 0.25 M films not only exhibit a smaller grain size but are generally more disordered structurally and also exhibit a higher degree of MA^+-induced polarization disorder than the 0.75 M films. Temperature-dependent Raman measurements were performed on both 0.25 and 0.75 M films (fig. S36). Interesting trends are observed upon tracking the peak positions of 90 and 220 cm^{-1} with temperature. Figure 4D shows the shift in the peak position corresponding to the torsional motion of MA^+ for the 0.25 and 0.75 M samples with temperature. As shown in Fig. 4D, both samples show significant softening of the

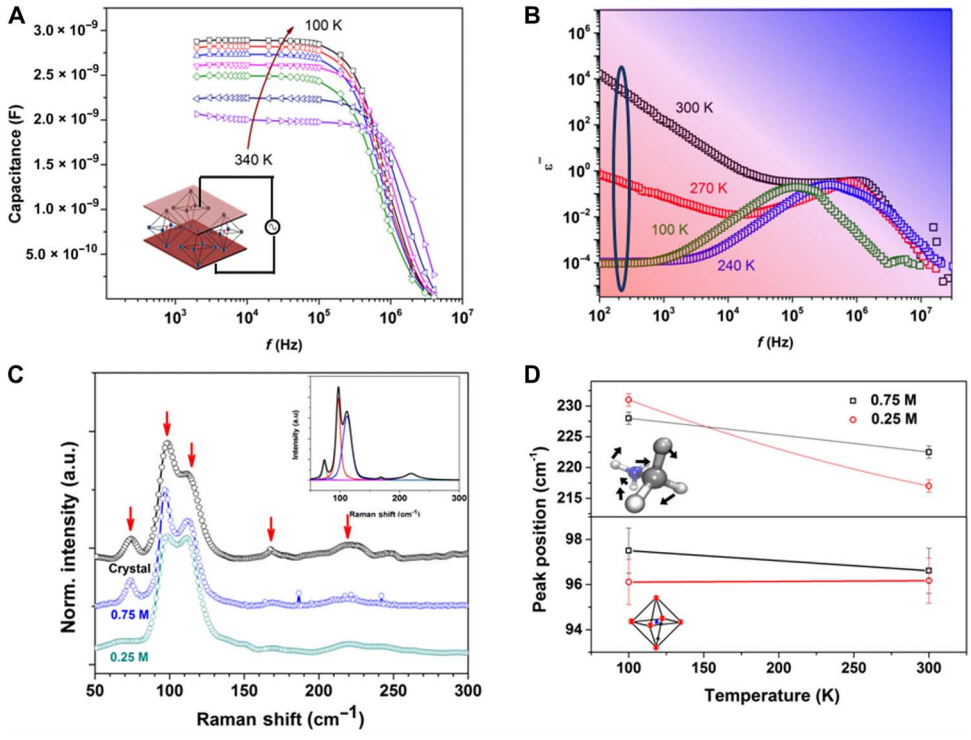

Fig. 4. Spectroscopic investigation of the sources of disorder in $MAPbI_3$ thin films. (**A**) Capacitance of 250-nm-thick perovskite thin films measured on an Au/perovskite/Au sandwich device (schematically shown in the inset) as a function of temperature in steps of 40 K with an applied ac voltage of 30 mV. (**B**) Corresponding dielectric loss measurement as a function of frequency and temperature. (**C**) Raman spectra for 0.75 and 0.25 M perovskite thin films as well as reference single crystals measured at room temperature with a 532-nm laser excitation. The inset shows the Lorentzian fits to the different peaks of the spectrum. a.u., arbitrary units. (**D**) Plot of the shift in peak position corresponding to the vibration mode of MA^+ and the Pb-I octahedron with temperature. The insets show a schematic representation of the corresponding molecular vibrations.

peak position with temperature; however, the degree of softening is more pronounced in the 0.25 M sample. Peak softening of 14 cm^{-1} was observed for films with small grain size (0.25 M) compared to a softening of 6 cm^{-1} for the films with larger crystallites (0.75 M). This observed pronounced softening of the peak with temperature is also consistent with a higher degree of MA^+ polarization disorder for perovskite samples with smaller grain size compared to films with larger grains (*48*–*50*). In the same temperature range, the peak position corresponding to the Pb-I does not exhibit significant shifts. This suggests that vibrations of the Pb-I cages may become the most important source of thermal disorder below ~165 ± 10 K in the orthorhombic phase where the MA^+ dipole moments become ordered (*45*).

Because the most significant reduction in the disorder of the MA^+ dipole moments occurs at temperatures above 160 K (Fig. 4A) (*45*, *51*), we propose that in regime II, the observed μ_{FET} temperature dependence is governed by the decrease in the MA^+ polarization disorder with decreasing temperature. The transition into regime I reflects a different carrier scattering mechanism with the weaker temperature dependence becoming dominant. We define the transition temperature $T_{I\text{-}II}$ between the two regimes, which is estimated from the intersection of the power-law fitting, in regime I and II. $T_{I\text{-}II}$ closely corresponds to the crystal phase transition in our perovskite films. The phase transition temperature was directly observed in our films to be 165 ± 10 K for all perovskite films, irrespective of the grain size, using temperature-dependent optical absorption spectroscopy (fig. S37). In the orthorhombic phase, the MA^+ dipoles are ordered (*45*, *51*, *52*), and one might expect carrier scattering to become dominated by the vibrations of the Pb-I cages to which electrons in the Pb 6p-like conduction band are expected to couple strongly (*50*). We emphasize that in contrast to the work of Duan *et al.* (*21*), we do not observe an abrupt step change in mobility that indicates the phase transition (*53*). This could possibly be attributed to the polycrystalline nature of thin films exhibiting broader phase transition temperatures in contrast to the well-defined phase transition temperature expected for single crystals (section S17).

In conclusion, with systematic control of grain size and contact interface engineering, it was possible to demonstrate high-performance perovskite FETs that exhibit clearly defined linear and saturation regime of the charge transport with μ_{FET} of ~0.5 cm^2/Vs at 300 K and >2 cm^2/Vs at 100 K, which approach, within an order of magnitude, local mobility values reported previously from THz and microwave conductivity measurements. A combination of structural and spectroscopic investigations were performed to probe the different sources of disorder prevalent in the perovskite field-effect transport. From the analysis, we attribute the enhanced charge transport and observation of room temperature field-effect transport to the combination of factors originating from the minimization of charged point defects located at grain boundaries, a decrease in the polarization fluctuation of the MA^+ cations with larger grain size, and appropriate contact engineering to induce crystalline order as well as isolate the S-D electrode from the perovskite. These strategies have not only allowed us to gain an insight into the different scattering mechanisms that govern the temperature-dependent transport physics of these materials but are

also likely to be important for achieving further improvements in device performance and extending FET charge transport studies to related classes of hybrid materials, such as 2D perovskites.

MATERIALS AND METHODS

Perovskite preparation

CH_3NH_3I was synthesized according to previously reported procedure (*2*). Absolute ethanol (100 ml) was used to dilute 24 ml of methylamine solution (33% in ethanol) in a 250-ml round bottom flask, followed by the addition of 10 ml of aqueous solution of hydriodic acid (57 weight %) under constant stirring. After 1 hour of reaction time at room temperature, a rotary evaporator was used to remove the solvents from the reaction mixture. The white solid residual was then washed using dry diethyl ether and recrystallized from ethanol to get methylammonium iodide crystals (CH_3NH_3I). Lead(II) acetate trihydrate (99.999%) was purchased from Sigma-Aldrich Inc. The precursor solution for fabricating thin films of perovskites was prepared by adding a 3:1 molar ratio of methylammonium iodide and lead acetate in *N*,*N*′-dimethylformamide to get 0.25, 0.50, and 0.75 M concentrations of perovskite precursor solutions, respectively. The perovskite films were spin-coated at 2000, 3000, and 5000 rpm for 0.25, 0.5, and 0.75 M, respectively, and annealed at 100°C for 5 min. Preparation of the perovskite thin films at different concentrations and spin speeds allowed the tuning of the crystallite size of the perovskite thin films as shown in the SEM images (Fig. 1A).

Device fabrication

The transport measurements were performed on a bottom-contact top-gate field-effect transistor. For the fabrication of the FETs Cr/Au (2 nm:20 nm), electrodes were evaporated and patterned by photolithography onto precleaned plasma-treated glass substrates onto which the perovskite layer was deposited as described above. A Cytop dielectric layer of thickness ~500 nm was spin-coated over the perovskite film and annealed at 90°C for 20 min. This was followed by the evaporation of the Au gate electrode (25 nm) through a shadow mask to complete the device. For the dual-gated devices, the perovskite layer is coated on lithographically patterned S-D electrodes over the Si/SiO_2 (300 nm) substrates. This was followed by spin-coating a Cytop layer and further coating the gate electrode in the same way as described earlier. All the devices, except the ones specified as continuous mode, were characterized using an Agilent 4155B parameter analyzer operated in pulsed mode. In the pulsed mode of operation, for the transfer (output) measurement V_g, (V_d) was applied over a short impulse of 0.5 ms. When the continuous mode of operation was used, the voltages were applied continuously in between measurements during the scan. The temperature-dependent transport measurements were performed using a Desert Cryogenics low-temperature probe station.

Impedance measurement

Sandwich devices were fabricated with patterned Au bottom electrode and shadow mask–patterned top Au electrode. To minimize leakage and obtain reliable devices, thicker perovskite films (>0.25 μm) were used. The spin-coated films were annealed at 100°C for 5 min. Impedance measurements were performed using a standard HP 4912A Impedance Analyzer over a frequency of 100 Hz to 10 MHz. The sample temperature was varied using a Desert Cryogenics low-temperature probe station.

Raman measurements

Raman spectroscopy measurements were performed on perovskite films fabricated on a quartz substrate. The Raman spectra were collected using a HORIBA T64000 Raman spectrometer attached to a confocal microscope with a 100× objective and a 532-nm laser for the excitation. Laser power was minimized to ensure that no degradation of the sample was induced. The spectra were recorded from 50 to 300 cm^{-1} and averaged over several accumulations. The samples were mounted on an Oxford Instruments MicrostatHiResII cryostat for temperature-dependent studies in the range of 10 to 300 K. The samples were cooled using a liquid helium cryostat while maintained at a vacuum of 10^{-6} mbar. Achieving significant signal-to-noise ratio while maintaining a sufficiently small laser intensity to avoid degradation of the sample was difficult at intermediate temperatures; hence, we only show here measurements at room temperature and low temperatures (100 K), where degradation induced peaks are not present (*54*).

SEM measurements

The surface of the perovskite films were imaged using an LEO Variable SEM. It was ensured that the voltage levels did not affect the integrity of the perovskite thin films.

Photothermal deflection spectroscopy

Samples were prepared in an identical fashion as used for the device fabrication on spectrosil quartz slides (which were cleaned with deionized water, acetone, and isopropanol followed by 10 min of oxygen plasma etch). The samples were kept in an airtight-sealed quartz cuvette filled with an inert liquid, Fluorinert FC-72 from 3M Corporation, which acts as the deflection medium with a large temperature-dependent refractive index. The perovskite thin films were excited with a modulated monochromatic light beam perpendicular to the plane of the sample obtained by a combination of a Light Support MKII 100W Xenon arc source and a CVI DK240 monochromator. The transverse probe beam was produced with a Qioptiq 670-nm fiber-coupled diode laser and passed as close as possible to the perovskite film surface. Beam deflection was measured using a differentially amplified quadrant photodiode and a Stanford Research SR830 lock-in amplifier, which is proportional to the absorption in the sample.

SUPPLEMENTARY MATERIALS

Supplementary material for this article is available at http://advances.sciencemag.org/cgi/content/full/3/1/e1601935/DC1

section S1. Characterization of the perovskite films
section S2. PbI_2 precursor–based perovskite FETs
section S3. Output characteristics of perovskite FETs
section S4. Mobility extraction for temperature-dependent transport measurements
section S5. Hysteresis in perovskite FETs
section S6. Detailed characteristics of Au-PFBT–based perovskite FETs
section S7. Role of interlayers at the S-D electrodes
section S8. Bias stress measurements on perovskite FETs
section S9. Transfer characteristics in continuous mode bias
section S10. Ferroelectric polarization measurement
section S11. Dielectric dependence of the hysteresis in transfer curves
section S12. Role of thermal cycling on the charge transport
section S13. Regimes of transport in $\mu_{FET}(T)$
section S14. Impedance spectroscopy
section S15. Estimation of Urbach energy (E_u) with temperature
section S16. Temperature-dependent Raman measurement
section S17. Temperature-dependent absorption measurement
fig. S1. Microscopic characterization.

fig. S2. XRD measured on different perovskite thin films.
fig. S3. High-resolution XRD indicating the assigned peaks for 0.25 M perovskite films.
fig. S4. Structural characterization.
fig. S5. PbI_2 precursor–based transistors.
fig. S6. Effect of grain size on FET characteristics.
fig. S7. Typical mobility extraction from linear fits to the $I_{ds}^{0.5}$ with V_g for V_d = 60 V.
fig. S8. Histograms of mobilities extracted from perovskite FETs fabricated from 0.75 M solution and PEIE-treated electrodes.
fig. S9. Hysteresis in output characteristics.
fig. S10. Close to room temperature characterization of dual-gated FETs.
fig. S11. Low-temperature characterization of dual-gated FETs.
fig. S12. Au-PFBT–treated FET characterization.
fig. S13. Characterization of interlayer treatment on electrodes.
fig. S14. SEM images of the perovskite thin films in different regions around the lithographically patterned pristine Au and modified Au S-D electrodes used for the FET fabrication.
fig. S15. SEM image of 0.5 M perovskite films depicting the difference in nucleation and grain size in the channel and on top of the electrodes near the channel-electrode interface for bare Au (left) and PEIE-treated S-D contacts.
fig. S16. XRD pattern obtained from the perovskite films (0.75 M precursor) fabricated on different substrates.
fig. S17. Stability towards bias stress.
fig. S18. Bias stress measurement of the output characteristics at different temperatures measured on perovskite FETs fabricated from 0.75 M precursor solution and Au S-D electrodes.
fig. S19. Bias stress measurement of the output characteristics at different temperatures measured on perovskite FETs fabricated from 0.75 M precursor solution and PEIE-treated Au S-D electrodes.
fig. S20. Temperature-dependent transfer characteristics measured at V_d = 60 V for perovskite FETs fabricated with 0.75 M precursor, Au-PEIE S-D electrode, and Cytop dielectric measured under a continuous mode of bias.
fig. S21. Representative polarization (P)–electric field (E) loops measured on an Au/perovskite (~0.7 μm)/Au sandwich device at different temperatures and frequency.
fig. S22. Normalized transfer curves for perovskite FET devices fabricated with 0.75 M Au-PEIE device with Cytop and PMMA dielectric layer.
fig. S23. Effect of V_d on FET hysteresis.
fig. S24. Effect of temperature cycling on the performance of a perovskite transistor fabricated with 0.75 M precursor solution, Cytop dielectric layer, and PFBT-treated Au S-D electrodes.
fig. S25. Transfer characteristics measured on perovskite devices (0.75 M; Au-PEIE–treated electrodes), indicating the effect of biasing at $V_g = V_d$ = 60 V on the FET performance during the first cycle of transistor performance.
fig. S26. Transfer characteristics measured on perovskite devices (0.75 M; Au-PEIE–treated electrodes) upon thermal cycling.
fig. S27. Transfer characteristics measured on perovskite devices (0.75 M; Au-PEIE–treated electrodes) while biasing during thermal cycling.
fig. S28. Effect of thermal cycling and bias on the capacitance of perovskite films measured at different temperature.
fig. S29. Effect of thermal cycling on energetic disorder in perovskite thin films.
fig. S30. Structural characterization of the perovskite thin films of different precursor concentrations upon thermal cycling.
fig. S31. Effect of thermal cycling on the perovskite grain size.
fig. S32. Transfer curves measured at 100 K from a FET fabricated with a 0.75 M Au-PEIE–treated S-D electrodes with Cytop dielectric layer depicting the effect of thermal cycling.
fig. S33. $\mu_{FET}(T)$ for perovskite transistors fabricated from perovskite films with different precursor concentration.
fig. S34. Temperature dependence impedance measurement.
fig. S35. Temperature-dependent disorder estimation in perovskite thin films.
fig. S36. Raman spectra measured on thin films fabricated with different grain size.
fig. S37. Temperature-dependent absorption measurements showing evidence of the phase transition from tetragonal to orthorhombic phase over the temperature range of 160 to 170 K for perovskite films of different grain sizes.

REFERENCES AND NOTES

1. M. M. Lee, J. Teuscher, T. Miyasaka, T. N. Murakami, H. J. Snaith, Efficient hybrid solar cells based on meso-superstructured organometal halide perovskites. *Science* **338**, 643–647 (2012).
2. A. Sadhanala, S. Ahmad, B. Zhao, N. Giesbrecht, P. M. Pearce, F. Deschler, R. L. Z. Hoye, K. C. Gödel, T. Bein, P. Docampo, S. E. Dutton, M. F. L. De Volder, R. H. Friend, Blue-green color tunable solution processable organolead chloride–bromide mixed halide perovskites for optoelectronic applications. *Nano Lett.* **15**, 6095–6101 (2015).
3. Z.-K. Tan, R. S. Moghaddam, M. L. Lai, P. Docampo, R. Higler, F. Deschler, M. Price, A. Sadhanala, L. M. Pazos, D. Credgington, F. Hanusch, T. Bein, H. J. Snaith, R. H. Friend, Bright light-emitting diodes based on organometal halide perovskite. *Nat. Nanotechnol.* **9**, 687–692 (2014).
4. W. Chen, Y. Wu, Y. Yue, J. Liu, W. Zhang, X. Yang, H. Chen, E. Bi, I. Ashraful, M. Grätzel, L. Han, Efficient and stable large-area perovskite solar cells with inorganic charge extraction layers. *Science* **350**, 944–948 (2015).
5. H. Cho, S.-H. Jeong, M.-H. Park, Y.-H. Kim, C. Wolf, C.-L. Lee, J. H. Heo, A. Sadhanala, N. Myoung, S. Yoo, S. H. Im, R. H. Friend, T.-W. Lee, Overcoming the electroluminescence efficiency limitations of perovskite light-emitting diodes. *Science* **350**, 1222–1225 (2015).
6. F. Deschler, M. Price, S. Pathak, L. E. Klintberg, D.-D. Jarausch, R. Higler, S. Hüttner, T. Leijtens, S. D. Stranks, H. J. Snaith, M. Atatüre, R. T. Phillips, R. H. Friend, High photoluminescence efficiency and optically pumped lasing in solution-processed mixed halide perovskite semiconductors. *J. Phys. Chem. Lett.* **5**, 1421–1426 (2014).
7. H. Zhu, Y. Fu, F. Meng, X. Wu, Z. Gong, Q. Ding, M. V. Gustafsson, M. T. Trinh, S. Jin, X.-Y. Zhu, Lead halide perovskite nanowire lasers with low lasing thresholds and high quality factors. *Nat. Mater.* **14**, 636–642 (2015).
8. S. D. Stranks, H. J. Snaith, Metal-halide perovskites for photovoltaic and light-emitting devices. *Nat. Nanotechnol.* **10**, 391–402 (2015).
9. A. Sadhanala, F. Deschler, T. H. Thomas, S. E. Dutton, K. C. Goedel, F. C. Hanusch, M. L. Lai, U. Steiner, T. Bein, P. Docampo, D. Cahen, R. H. Friend, Preparation of single-phase films of $CH_3NH_3Pb(I_{1-x}Br_x)_3$ with sharp optical band edges. *J. Phys. Chem. Lett.* **5**, 2501–2505 (2014).
10. D. Shi, V. Adinolfi, R. Comin, M. Yuan, E. Alarousu, A. Buin, Y. Chen, S. Hoogland, A. Rothenberger, K. Katsiev, Y. Losovyj, X. Zhang, P. A. Dowben, O. F. Mohammed, E. H. Sargent, O. M. Bakr, Low trap-state density and long carrier diffusion in organolead trihalide perovskite single crystals. *Science* **347**, 519–522 (2015).
11. A. Miyata, A. Mitioglu, P. Plochocka, O. Portugall, J. T.-W. Wang, S. D. Stranks, H. J. Snaith, R. J. Nicholas, Direct measurement of the exciton binding energy and effective masses for charge carriers in organic–inorganic tri-halide perovskites. *Nat. Phys.* **11**, 582–587 (2015).
12. M. B. Johnston, L. M. Herz, Hybrid perovskites for photovoltaics: Charge-carrier recombination, diffusion, and radiative efficiencies. *Acc. Chem. Res.* **49**, 146–154 (2016).
13. T. M. Brenner, D. A. Egger, L. Kronik, G. Hodes, D. Cahen, Hybrid organic—Inorganic perovskites: Low-cost semiconductors with intriguing charge-transport properties. *Nat. Rev. Mater.* **2016**, 16011 (2016).
14. H. Sirringhaus, M. Bird, N. Zhao, Charge transport physics of conjugated polymer field-effect transistors. *Adv. Mater.* **22**, 3893–3898 (2010).
15. H. Sirringhaus, Device physics of solution-processed organic field-effect transistors. *Adv. Mater.* **17**, 2411–2425 (2005).
16. B. Radisavljevic, A. Kis, Mobility engineering and a metal–insulator transition in monolayer MoS_2. *Nat. Mater.* **12**, 815–820 (2013).
17. C. R. Kagan, D. B. Mitzi, C. D. Dimitrakopoulos, Organic–inorganic hybrid materials as semiconducting channels in thin-film field-effect transistors. *Science* **286**, 945–947 (1999).
18. X. Y. Chin, D. Cortecchia, J. Yin, A. Bruno, C. Soci, Lead iodide perovskite light-emitting field-effect transistor. *Nat. Commun.* **6**, 7383 (2015).
19. F. Li, C. Ma, H. Wang, W. Hu, W. Yu, A. D. Sheikh, T. Wu, Ambipolar solution-processed hybrid perovskite phototransistors. *Nat. Commun.* **6**, 8238 (2015).
20. Y. Mei, C. Zhang, Z. V. Vardeny, O. D. Jurchescu, Electrostatic gating of hybrid halide perovskite field-effect transistors: Balanced ambipolar transport at room-temperature. *MRS Commun.* **5**, 297–301 (2015).
21. D. Li, G. Wang, H.-C. Cheng, C.-Y. Chen, H. Wu, Y. Liu, Y. Huang, X. Duan, Size-dependent phase transition in methylammonium lead iodide perovskite microplate crystals. *Nat. Commun.* **7**, 11330 (2016).
22. J. G. Labram, D. H. Fabini, E. E. Perry, A. J. Lehner, H. Wang, A. M. Glaudell, G. Wu, H. Evans, D. Buck, R. Cotta, L. Echegoyen, F. Wudl, R. Seshadri, M. L. Chabinyc, Temperature-dependent polarization in field-effect transport and photovoltaic measurements of methylammonium lead iodide. *J. Phys. Chem. Lett.* **6**, 3565–3571 (2015).
23. G. Wang, D. Li, H.-C. Cheng, Y. Li, C.-Y. Chen, A. Yin, Z. Zhao, Z. Lin, H. Wu, Q. He, M. Ding, Y. Liu, Y. Huang, X. Duan, Wafer-scale growth of large arrays of perovskite microplate crystals for functional electronics and optoelectronics. *Sci. Adv.* **1**, e1500613 (2015).
24. J.-H. Im, I.-H. Jang, N. Pellet, M. Grätzel, N.-G. Park, Growth of $CH_3NH_3PbI_3$ cuboids with controlled size for high-efficiency perovskite solar cells. *Nat. Nanotechnol.* **9**, 927–932 (2014).
25. W. Zhang, M. Saliba, D. T. Moore, S. K. Pathak, M. T. Hörantner, T. Stergiopoulos, S. D. Stranks, G. E. Eperon, J. A. Alexander-Webber, A. Abate, A. Sadhanala, S. Yao, Y. Chen, R. H. Friend, L. A. Estroff, U. Wiesner, H. J. Snaith, Ultrasmooth organic–inorganic perovskite thin-film formation and crystallization for efficient planar heterojunction solar cells. *Nat. Commun.* **6**, 6142 (2015).
26. J. Burschka, N. Pellet, S.-J. Moon, R. Humphry-Baker, P. Gao, M. K. Nazeeruddin, M. Grätzel, Sequential deposition as a route to high-performance perovskite-sensitized solar cells. *Nature* **499**, 316–319 (2013).
27. A. Buin, P. Pietsch, J. Xu, O. Voznyy, A. H. Ip, R. Comin, E. H. Sargent, Materials processing routes to trap-free halide perovskites. *Nano Lett.* **14**, 6281–6286 (2014).

28. Y. Shao, Y. Fang, T. Li, Q. Wang, Q. Dong, Y. Deng, Y. Yuan, H. Wei, M. Wang, A. Gruverman, J. Shield, J. Huang, Grain boundary dominated ion migration in polycrystalline organic–inorganic halide perovskite films. *Energ. Environ. Sci.* **9**, 1752–1759 (2016).
29. Y. Zhou, C. Fuentes-Hernandez, J. Shim, J. Meyer, A. J. Giordano, H. Li, P. Winget, T. Papadopoulos, H. Cheun, J. Kim, M. Fenoll, A. Dindar, W. Haske, E. Najafabadi, T. M. Khan, H. Sojoudi, S. Barlow, S. Graham, J.-L. Brédas, S. R. Marder, A. Kahn, B. Kippelen, A universal method to produce low–work function electrodes for organic electronics. *Science* **336**, 327–332 (2012).
30. H. Oga, A. Saeki, Y. Ogomi, S. Hayase, S. Seki, Improved understanding of the electronic and energetic landscapes of perovskite solar cells: High local charge carrier mobility, reduced recombination, and extremely shallow traps. *J. Am. Chem. Soc.* **136**, 13818–13825 (2014).
31. Z.-K. Wang, X. Gong, M. Li, Y. Hu, J.-M. Wang, H. Ma, L.-S. Liao, Induced crystallization of perovskites by a perylene underlayer for high-performance solar cells. *ACS Nano* **10**, 5479–5489 (2016).
32. D. J. Gundlach, J. E. Royer, S. K. Park, S. Subramanian, O. D. Jurchescu, B. H. Hamadani, A. J. Moad, R. J. Kline, L. C. Teague, O. Kirillov, C. A. Richter, J. G. Kushmerick, L. J. Richter, S. R. Parkin, T. N. Jackson, J. E. Anthony, Contact-induced crystallinity for high-performance soluble acene-based transistors and circuits. *Nat. Mater.* **7**, 216–221 (2008).
33. C. Eames, J. M. Frost, P. R. F. Barnes, B. C. O'Regan, A. Walsh, M. S. Islam, Ionic transport in hybrid lead iodide perovskite solar cells. *Nat. Commun.* **6**, 7497 (2015).
34. S. Meloni, T. Moehl, W. Tress, M. Franckevičius, M. Saliba, Y. H. Lee, P. Gao, M. K. Nazeeruddin, S. M. Zakeeruddin, U. Rothlisberger, M. Graetzel, Ionic polarization-induced current–voltage hysteresis in $CH_3NH_3PbX_3$ perovskite solar cells. *Nat. Commun.* **7**, 10334 (2016).
35. A. Filippetti, P. Delugas, M. I. Saba, A. Mattoni, Entropy-suppressed ferroelectricity in hybrid lead-iodide perovskites. *J. Phys. Chem. Lett.* **6**, 4909–4915 (2015).
36. W.-Q. Liao, Y. Zhang, C.-L. Hu, J.-G. Mao, H.-Y. Ye, P.-F. Li, S. D. Huang, R.-G. Xiong, A lead-halide perovskite molecular ferroelectric semiconductor. *Nat. Commun.* **6**, 7338 (2015).
37. H.-W. Chen, N. Sakai, M. Ikegami, T. Miyasaka, Emergence of hysteresis and transient ferroelectric response in organo-lead halide perovskite solar cells. *J. Phys. Chem. Lett.* **6**, 164–169 (2015).
38. E. J. Juarez-Perez, R. S. Sanchez, L. Badia, G. Garcia-Belmonte, Y. S. Kang, I. Mora-Sero, J. Bisquert, Photoinduced giant dielectric constant in lead halide perovskite solar cells. *J. Phys. Chem. Lett.* **5**, 2390–2394 (2014).
39. M. Bag, L. A. Renna, R. Y. Adhikari, S. Karak, F. Liu, P. M. Lahti, T. P. Russell, M. T. Tuominen, D. Venkataraman, Kinetics of ion transport in perovskite active layers and its implications for active layer stability. *J. Am. Chem. Soc.* **137**, 13130–13137 (2015).
40. M. N. F. Hoque, M. Yang, Z. Li, N. Islam, X. Pan, K. Zhu, Z. Fan, Polarization and dielectric study of methylammonium lead iodide thin film to reveal its nonferroelectric nature under solar cell operating conditions. *ACS Energy Lett.* **1**, 142–149 (2016).
41. D. H. Fabini, T. Hogan, H. A. Evans, C. C. Stoumpos, M. G. Kanatzidis, R. Seshadri, Dielectric and thermodynamic signatures of low-temperature glassy dynamics in the hybrid perovskites $CH_3NH_3PbI_3$ and $HC(NH_2)_2PbI_3$. *J. Phys. Chem. Lett.* **7**, 376–381 (2016).
42. Q. Lin, A. Armin, R. C. R. Nagiri, P. L. Burn, P. Meredith, Electro-optics of perovskite solar cells. *Nat. Photonics* **9**, 106–112 (2015).
43. C. C. Stoumpos, C. D. Malliakas, M. G. Kanatzidis, Semiconducting tin and lead iodide perovskites with organic cations: Phase transitions, high mobilities, and near-infrared photoluminescent properties. *Inorg. Chem.* **52**, 9019–9038 (2013).
44. N. Onoda-Yamamuro, T. Matsuo, H. Suga, Dielectric study of $CH_3NH_3PbX_3$ (X = Cl, Br, I). *J. Phys. Chem. Solid* **53**, 935–939 (1992).
45. A. M. A. Leguy, J. M. Frost, A. P. McMahon, V. G. Sakai, W. Kockelmann, C. Law, X. Li, F. Foglia, A. Walsh, B. C. O'Regan, J. Nelson, J. T. Cabral, P. R. F. Barnes, The dynamics of methylammonium ions in hybrid organic–inorganic perovskite solar cells. *Nat. Commun.* **6**, 7124 (2015).
46. A. A. Bakulin, O. Selig, H. J. Bakker, Y. L. A. Rezus, C. Müller, T. Glaser, R. Lovrincic, Z. Sun, Z. Chen, A. Walsh, J. M. Frost, T. L. C. Jansen, Real-time observation of organic cation reorientation in methylammonium lead iodide perovskites. *J. Phys. Chem. Lett.* **6**, 3663–3669 (2015).
47. C. Quarti, G. Grancini, E. Mosconi, P. Bruno, J. M. Ball, M. M. Lee, H. J. Snaith, A. Petrozza, F. De Angelis, The Raman spectrum of the $CH_3NH_3PbI_3$ hybrid perovskite: Interplay of theory and experiment. *J. Phys. Chem. Lett.* **5**, 279–284 (2014).
48. G. Grancini, S. Marras, M. Prato, C. Giannini, C. Quarti, F. De Angelis, M. De Bastiani, G. E. Eperon, H. J. Snaith, L. Manna, A. Petrozza, The impact of the crystallization processes on the structural and optical properties of hybrid perovskite films for photovoltaics. *J. Phys. Chem. Lett.* **5**, 3836–3842 (2014).
49. G. Grancini, A. R. S. Kandada, J. M. Frost, A. J. Barker, M. De Bastiani, M. Gandini, S. Marras, G. Lanzani, A. Walsh, A. Petrozza, Role of microstructure in the electron–hole interaction of hybrid lead halide perovskites. *Nat. Photonics* **9**, 695–701 (2015).
50. A. Walsh, D. O. Scanlon, S. Chen, X. G. Gong, S.-H. Wei, Self-regulation mechanism for charged point defects in hybrid halide perovskites. *Angew. Chem. Int. Ed.* **54**, 1791–1794 (2015).
51. M. T. Weller, O. J. Weber, P. F. Henry, A. M. Di Pumpo, T. C. Hansen, Complete structure and cation orientation in the perovskite photovoltaic methylammonium lead iodide between 100 and 352 K. *Chem. Commun.* **51**, 4180–4183 (2015).
52. V. D'Innocenzo, G. Grancini, M. J. P. Alcocer, A. R. S. Kandada, S. D. Stranks, M. M. Lee, G. Lanzani, H. J. Snaith, A. Petrozza, Excitons versus free charges in organo-lead tri-halide perovskites. *Nat. Commun.* **5**, 3586 (2014).
53. H. T. Yi, X. Wu, X. Zhu, V. Podzorov, Intrinsic charge transport across phase transitions in hybrid organo-inorganic perovskites. *Adv. Mater.* **28**, 6509–6514 (2016).
54. M. Ledinský, P. Löper, B. Niesen, J. Holovský, S.-J. Moon, J.-H. Yum, S. De Wolf, A. Fejfar, C. Ballif, Raman spectroscopy of organic–inorganic halide perovskites. *J. Phys. Chem. Lett.* **6**, 401–406 (2015).
55. N. M. Kirby, S. T. Mudie, A. M. Hawley, D. J. Cookson, H. D. T. Mertens, N. Cowieson, V. Samardzic-Boban, A low-background-intensity focusing small-angle X-ray scattering undulator beamline. *J. Appl. Cryst.* **46**, 1670–1680 (2013).
56. D. Korolkov, P. Busch, L. Willner, E. Kentzinger, U. Rücker, A. Paul, H. Frielinghaus, T. Brückel, Analysis of randomly oriented structures by grazing-incidence small-angle neutron scattering. *J. Appl. Cryst.* **45**, 245–254 (2012).

Acknowledgments: S.P.S. and B.Y. acknowledge useful discussion with K. Broch on GIWAXS measurements. S.P.S. and T.H.T. acknowledge the help of T. B. Kehoe in Raman measurements. S.P.S. acknowledges N. Tiwale for help in SEM measurements. **Funding:** S.P.S. acknowledges funding from the Royal Society London for a Newton Fellowship. B.Y. acknowledges support from China Council Scholarship and Cambridge Overseas Trust. A.S. and R.H.F. acknowledge funding and support from the Engineering and Physical Sciences Research Council (EPSRC) through the India-U.K. APEX project. P.D. acknowledges support from the European Union through the award of a Marie Curie Intra-European Fellowship. X.M. is grateful for the support from the Royal Society. B.N. is grateful for the support from Gates Cambridge and the Winton Program for the Physics of Sustainability. We acknowledge funding from the EPSRC through a program grant (EP/M005143/1). We acknowledge funding from the German Federal Ministry of Education and Research under agreement number 01162525/1. This work was performed in part on the SAXS/WAXS beamline of the Australian Synchrotron, Victoria, Australia (*55*, *56*). C.R.M. acknowledges support from the Australian Research Council (DP13012616). **Author contributions:** S.P.S. and B.Y. performed, developed, and designed the experiments on FET, fabricated all the devices, and wrote the manuscript with significant inputs from H.S. on the manuscript, data analysis, and design. H.S., B.Y., and A.S. were involved in the initial conceptualization, design, and implementation of this work. A.S. performed the PDS measurements and analysis. T.H.T. performed the Raman measurements. S.G. provided inputs on Raman measurements. N.G. and P.D. synthesized the MAI. W.H., E.G., and C.R.M. performed the GIWAXS measurement. T.H.T. and K.G. performed the XRD measurements on the thin films. B.N. and X.M. performed the ferroelectric measurements. R.H.F. and H.S. supervised the work. All authors discussed the results and revised the manuscript. **Competing interests:** The authors declare that they have no competing interests. **Data availability:** All data needed to evaluate the conclusions in the paper are present in the paper and/or the Supplementary Materials. Additional data related to this paper may be requested from the authors.

Submitted 16 August 2016
Accepted 21 December 2016
Published 27 January 2017
10.1126/sciadv.1601935

Citation: S. P. Senanayak, B. Yang, T. H. Thomas, N. Giesbrecht, W. Huang, E. Gann, B. Nair, K. Goedel, S. Guha, X. Moya, C. R. McNeill, P. Docampo, A. Sadhanala, R. H. Friend, H. Sirringhaus, Understanding charge transport in lead iodide perovskite thin-film field-effect transistors. *Sci. Adv.* **3**, e1601935 (2017).

Science Advances

Understanding charge transport in lead iodide perovskite thin-film field-effect transistors

Satyaprasad P. Senanayak, Bingyan Yang, Tudor H. Thomas, Nadja Giesbrecht, Wenchao Huang, Eliot Gann, Bhaskaran Nair, Karl Goedel, Suchi Guha, Xavier Moya, Christopher R. McNeill, Pablo Docampo, Aditya Sadhanala, Richard H. Friend and Henning Sirringhaus

Sci Adv **3** (1), e1601935.
DOI: 10.1126/sciadv.1601935